

# The Dimensional Reduction Modelling Approach for 3D Beams: Differential Equations and Finite-Element Solutions Based on Hellinger-Reissner Principle

Ferdinando Auricchio<sup>a,b,c,d</sup>, Giuseppe Balduzzi<sup>a,e,\*</sup>, Carlo Lovadina<sup>c,d,e</sup>

<sup>a</sup>*Dipartimento di Ingegneria Civile e Architettura (DICAr), Università degli Studi di Pavia, Pavia, Italy*

<sup>b</sup>*European Centre for Training and Research in Earthquake Engineering (EUCENTRE), Pavia, Italy*

<sup>c</sup>*Istituto di Matematica Applicata e Tecnologie Informatiche (IMATI), CNR, Pavia, Italy*

<sup>d</sup>*Centro di Simulazione Numerica Avanzata (CeSNA), IUSS, Pavia, Italy*

<sup>e</sup>*Dipartimento di Matematica "Felice Casorati", Università degli Studi di Pavia, Pavia, Italy*

---

## Abstract

This paper illustrates an application of the so-called *dimensional reduction* modelling approach to obtain a mixed, 3D, linear, elastic beam-model.

We start from the *3D linear elastic problem*, formulated through the Hellinger-Reissner functional, then we introduce a cross-section piecewise-polynomial approximation, and finally we integrate within the cross section, obtaining a *beam model* that satisfies the cross-section equilibrium and could be applied to inhomogeneous bodies with also a non trivial geometries (such as L-shape cross section). Moreover the beam model can predict the local effects of both boundary displacement constraints and non homogeneous or concentrated boundary load distributions, usually not accurately captured by most of the popular beam models.

We modify the beam-model formulation in order to satisfy the axial compatibility (and without violating equilibrium within the cross section), then we introduce axis piecewise-polynomial approximation, and finally we integrate along the beam axis, obtaining a *beam finite element*. Also the beam finite elements have the capability to describe local effects of constraints and loads. Moreover, the proposed beam finite element describes the stress distribution inside the cross section with high accuracy.

In addition to the simplicity of the derivation procedure and the very satisfying numerical performances, both the beam model and the beam finite element can be refined arbitrarily, allowing to adapt the model accuracy to specific needs of practitioners.

*Keywords:* linear elastic beam, mixed variational modelling, beam analytical solution, static analysis, finite element

---

## 1. Introduction

The modelling of a *beam body*, i.e. a 3D, prismatic, slender, linear, and elastic body, is one of the most investigated problem in the continuum mechanics field. Nevertheless, this research area continues to be open to new contributions since new design-philosophies (e.g. the limit-states or the performance-based designs) and new technologies (e.g. composite materials) need more and more accurate analysis. Readers may refer to (Hjelmstad and Taciroglu, 2003) to get the idea about recent trends and discussions in beam-modelling field.

The *Euler-Bernoulli (EB) beam model*, proposed in eighteenth century, is a simple beam model, still widely used by practitioners, despite today's computational instruments allow to handle more refined models. In EB beam model, the cross section is forced to remain rigid and orthogonal to the beam axis, also in

---

\*Dipartimento di Matematica "Felice Casorati", via Ferrata 1, 27100 Pavia Italy  
Email address: giuseppe.balduzzi@unipv.it (Giuseppe Balduzzi)

deformed configuration. It follows that 4 cross-section rigid motion (i.e.: (i) the axial displacement; (ii-iii) the translations orthogonal to the beam axis; (iv) the rotation around the beam axis) are necessary to describe the beam kinematic and 4 independent Ordinary Differential Equations (ODEs) impose the equilibrium between the internal resulting stresses (i.e.: axial compression, shears, bending moments, and torque) and the applied loads.

However, EB beam is effective only for extremely slender bodies. As a consequence, in the past century, researchers developed many *refined beam models*. In the following we list a few significant examples, detailing improvements with respect to the EB beam model.

- *Timoshenko beam model*. It does not force the cross section to remain orthogonal to the beam axis and it solves the shear-bending problems more accurately (see e.g. (Timoshenko and Goodier, 1951)).
- *Higher order beam models*. They consider more refined kinematics. As an example, they assume that the cross section can warp and/or change shape (among the others, see e.g. (Vinayak et al., 1996)).
- *Mixed beam models*. They consider both displacement and stress as independent variables with the aim to improve the stress description (see (Hjelmstad and Taciroglu, 2002) for a brief introduction and a literature review).

Unfortunately, to be effective, many refined beam models and also the EB beam model require *stiffness correction factors* that are not easy to evaluate, in relatively simple cases, too.

In the nineteenth century, *Saint-Venant* (SV) proposed a completely different approach to beam modelling, i.e. he provided the solution of the continuum mechanic problem for a beam body assuming that: (i) the body is homogeneous and isotropic; (ii) no distributed-loads are applied; (iii) loads and displacement constraints are applied far from the region where the solution is evaluated; (iv) stress components orthogonal to the beam axis are negligible. Unfortunately, SV solution is not explicit because it depends on some unknown *warping functions*, governed by auxiliary Partial Differential Equations (PDEs) defined on the cross section. Readers may refer to (Timoshenko and Goodier, 1951) for more details.

Warping functions are deeply investigated not only in order to determine the SV solution, but also because they are useful in the evaluation of stiffness correction factors. As an example, Gruttmann et al. (1999) discuss the physical meaning of the warping functions and propose a numerical approach to solve the auxiliary PDEs, comparing some numerical results with available analytical solutions. More recently, Lacarbonara and Paolone (2007) propose and compare different strategies to compute the warping functions, highlighting advantages and critical steps of each strategy. In general, the numerical computation of warping functions could be quite expensive. However, it must be done only once, after the section geometry definition. As a consequence, the procedure is usually adopted in frame-structure analysis.

In practical applications, many of the hypotheses that allow to obtain the SV solution could be too restrictive. An attempt to overcome the SV hypotheses was proposed by Ladeveze and Simmonds (1998), under the assumption that the cross-section is a piecewise constant function along the beam axis. The 3D solution is obtained applying the 3 steps listed in the following: (i) definition of the beam-model constitutive operators through the solution of problems defined in the cross section, (ii) determination of the beam-model solution governed by a 1D problem, and (iii) reconstruction of the 3D solution through the combination of the constitutive operators. In addition to the SV solution, the resulting solution takes into account also *local effects* like stress concentrations that occur in proximity of displacement constrained boundary. As specified in (Ladeveze and Simmonds, 1998), the proposed theory determines exact static and kinematic generalized quantities (i.e. axial compression, shears, bending moments, torque, and the dual kinematic variables).

A completely different attempt to overcome the SV hypotheses in beam model formulation was proposed by Dong et al. (2001); Kosmatka et al. (2001) and Lin et al. (2001), that apply the *dimensional reduction method* to the continuum mechanic PDEs problem in order to obtain a semi-analytical SV-like solution. The authors assume displacement as independent variable and the Total Potential Energy variational principle as starting point in derivation whereas no restrictive hypotheses on materials, stress description, and loads are considered. Some ODEs govern the resulting model solution that describes effectively also local effects. The advantages of the approach are: (i) the procedure does not need the a-priori definition and solution of

auxiliary problems, (ii) stiffness coefficient factors are automatically computed through the model derivation procedure, and (iii) the description of boundary effects result as a component of the homogeneous solution of the ODEs governing the beam model problem.

It is worth mentioning that the dimensional reduction method was proposed by Kantorovich and Krylov (1958) as a general mathematical procedure that exploits the geometry of the domain to reduce the problem dimension (in beam modelling from 3D PDEs to ODEs). The method is widely used in continuum mechanic and we would cite, among other examples, (Vogelius and Babuska, 1981a,b; Alessandrini et al., 1999; Batra et al., 2002), and Batra and Vidoli (2002).

Recently, Auricchio et al. (2010) considered a *planar beam problem* and the *Hellinger-Reissner (HR) variational principle* as the starting point for the dimensional reduction procedure. By choosing appropriate cross-section approximating profiles, the resulting beam model is capable, in particular, of accurately describing the cross-section stress distribution. In addition, Auricchio et al. (2010) proposed a suitable FE approximation of that beam model.

In this paper, we generalize the approach and the FE derivation procedure illustrated in Auricchio et al. (2010) to a *3D beam body*. Due to the 2D nature of the cross-sections, the choice of the approximating profiles requires more care than the corresponding planar case.

A brief outline of the paper is as follows. In Section 2 we define the problem we are interested in, and in Section 3 we derive the beam model starting from the HR functional, giving also some insight on the structure of its analytical solution. In Section 4 we develop suitable FE schemes, and in Section 5 we present numerical results to illustrate the actual computational performances of our approach.

## 2. Problem definition

We consider a 3D, prismatic, slender, linear, and elastic body under the hypothesis of small displacements. For simplicity, we consider only isotropic materials, even if this assumption is not necessary for the model derivation.

We define the problem domain as:

$$\Omega := l \times A \tag{1}$$

where the beam longitudinal axis  $l \subset \mathbb{R}$  and the cross section  $A \subset \mathbb{R}^2$  are orthogonal, closed and bounded sets. Figure 1 represents the domain  $\Omega$ , the adopted Cartesian coordinate system, the initial and final cross

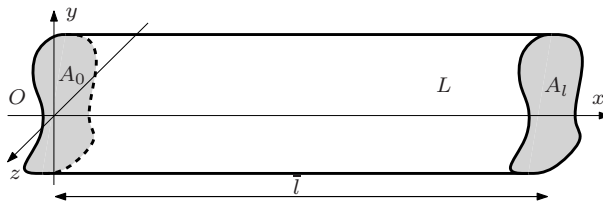


Figure 1: 3D beam body geometry, coordinate system, dimensions, and adopted notations.

sections ( $A_0$  and  $A_l$  respectively), and the lateral surface  $L := \partial A \times l$ , where  $\partial A$  is the boundary of the cross section, as illustrated in Figure 2. Thus, the domain boundary is  $\partial\Omega := A_0 \cup A_l \cup L$  and we consider the partition  $\{\partial\Omega_t; \partial\Omega_s\}$ , where  $\partial\Omega_t$  and  $\partial\Omega_s$  are the externally loaded and the displacement constrained boundaries, respectively. We notice that the body could be inhomogeneous in the cross section, as illustrated in Figure 2. As a consequence, the Young's modulus  $E$  and the Poisson's ratio  $\nu$  are scalar fields depending on the cross-section coordinates, i.e.  $E : A \rightarrow \mathbb{R}$  and  $\nu : A \rightarrow \mathbb{R}$ .

The prescribed boundary displacement  $\bar{\mathbf{s}} : \partial\Omega_s \rightarrow \mathbb{R}^3$ , the external load, defined as a surface force density  $\mathbf{t} : \partial\Omega_t \rightarrow \mathbb{R}^3$ , and the body load, defined as a volume force density  $\mathbf{f} : \Omega \rightarrow \mathbb{R}^3$ , are assumed to be sufficiently smooth functions.

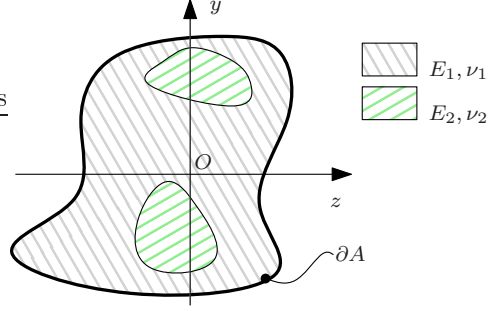


Figure 2: Cross section geometry, coordinate system, and adopted notations.

Introducing the symmetric stress tensor field  $\boldsymbol{\sigma} : \Omega \rightarrow \mathbb{R}_s^{3 \times 3}$ , the displacement vector field  $\mathbf{s} : \Omega \rightarrow \mathbb{R}^3$ , the corresponding variation fields  $\delta \boldsymbol{\sigma}$  and  $\delta \mathbf{s}$ , and the following spaces:

$$\begin{aligned}
 L^2(\Omega) &:= \{ \mathbf{s} : \Omega \rightarrow \mathbb{R}^3 : \int_{\Omega} \mathbf{s} \cdot \mathbf{s} \, d\Omega < \infty \} \\
 H(\text{div}, \Omega) &:= \{ \boldsymbol{\sigma} : \Omega \rightarrow \mathbb{R}_s^{3 \times 3} : \int_{\Omega} \boldsymbol{\sigma} : \boldsymbol{\sigma} \, d\Omega < \infty \text{ and } (\nabla \cdot \boldsymbol{\sigma}) \in L^2(\Omega) \} \\
 W &:= \{ \mathbf{s} \in L^2(\Omega) \} \\
 S_t &:= \{ \boldsymbol{\sigma} \in H(\text{div}, \Omega) : \boldsymbol{\sigma} \cdot \mathbf{n}|_{\partial\Omega_t} = \mathbf{t} \} \\
 S_0 &:= \{ \delta \boldsymbol{\sigma} \in H(\text{div}, \Omega) : \delta \boldsymbol{\sigma} \cdot \mathbf{n}|_{\partial\Omega_t} = \mathbf{0} \}
 \end{aligned} \tag{2}$$

the 3D elastic problem consists in solving the following variational system.

$$\begin{aligned}
 &\text{Find } \mathbf{s} \in W \text{ and } \boldsymbol{\sigma} \in S_t \text{ such that } \forall \delta \mathbf{s} \in W \\
 &\text{and } \forall \delta \boldsymbol{\sigma} \in S_0 \\
 \delta J_{HR} &:= - \int_{\Omega} \delta \mathbf{s} \cdot \nabla \cdot \boldsymbol{\sigma} \, d\Omega - \int_{\Omega} \nabla \cdot \delta \boldsymbol{\sigma} \cdot \mathbf{s} \, d\Omega - \int_{\Omega} \delta \boldsymbol{\sigma} : \mathbf{D}^{-1} : \boldsymbol{\sigma} \, d\Omega - \int_{\Omega} \delta \mathbf{s} \cdot \mathbf{f} \, d\Omega \\
 &+ \int_{\partial\Omega_s} \delta \boldsymbol{\sigma} \cdot \mathbf{n} \cdot \bar{\boldsymbol{\sigma}} \, dA = 0
 \end{aligned} \tag{3}$$

Above,  $\mathbf{D}$  is the fourth order, linear, elastic, isotropic tensor which depends on the material parameters  $E$  and  $\nu$ .

We highlight that, due to the adopted formulation, the boundary equilibrium  $\boldsymbol{\sigma} \cdot \mathbf{n}|_{\partial\Omega_t} = \mathbf{t}$  is an *essential* condition, i.e. it is directly inserted into the definition of the trial space  $S_t$ . On the contrary, the boundary compatibility  $\mathbf{s}|_{\partial\Omega_s} = \bar{\boldsymbol{\sigma}}$  is a *natural* condition, i.e. it is weakly imposed to the solution component  $\mathbf{s}$  through the variational system (3).

### 3. Model derivation

In this section, starting from the 3D problem weak formulation (3), we perform the dimensional reduction which is based on the introduction of field cross-section approximations and on a cross-section integration. For simplicity, in the model derivation, we switch to an engineering-oriented notation.

#### 3.1. Cross-section approximation and notations

The first step in the beam model derivation is to approximate the generic three-dimensional field  $\gamma : \Omega \rightarrow \mathbb{R}^{(\cdot)}$  as a linear combination of  $d$  *cross-section shape functions*, stored in a vector  $\mathbf{r}_{\gamma} : A \rightarrow \mathbb{R}^{(\cdot) \times d}$ ,

weighted with arbitrary *axial coefficient functions*  $\hat{\boldsymbol{\gamma}} : l \rightarrow \mathbb{R}^d$ , i.e. formally:

$$\boldsymbol{\gamma}(x, y, z) \approx \mathbf{r}_\gamma^T(y, z) \hat{\boldsymbol{\gamma}}(x) \quad (4)$$

where  $(\cdot)^T$  indicates the transposition operation.

We emphasize that the cross-section shape functions  $\mathbf{r}_\gamma(y, z)$  are a set of pre-assigned, linearly-independent functions. As a consequence, the field  $\boldsymbol{\gamma}(x, y, z)$  is uniquely determined by the axial coefficient functions  $\hat{\boldsymbol{\gamma}}(x)$  that are indeed the *unknowns* of the beam model we are developing. In the following, we omit the dependences of  $\mathbf{r}_\gamma$  on  $y, z$  and of  $\hat{\boldsymbol{\gamma}}$  on  $x$  for notation simplicity.

Adopting Position (4) and switching to an engineering notation we set:

$$\mathbf{s} := \begin{Bmatrix} s_u \\ s_v \\ s_w \end{Bmatrix} \approx \begin{bmatrix} \mathbf{r}_u^T & \mathbf{0} & \mathbf{0} \\ \mathbf{0} & \mathbf{r}_v^T & \mathbf{0} \\ \mathbf{0} & \mathbf{0} & \mathbf{r}_w^T \end{bmatrix} \begin{Bmatrix} \hat{\mathbf{u}} \\ \hat{\mathbf{v}} \\ \hat{\mathbf{w}} \end{Bmatrix} = \mathbf{R}_s \hat{\mathbf{s}} \quad (5)$$

$$\boldsymbol{\sigma} := \{\sigma_{xx}, \sigma_{yy}, \sigma_{zz}, \tau_{xy}, \tau_{xz}, \tau_{yz}\}^T \approx \begin{bmatrix} \mathbf{r}_{\sigma_x}^T & \mathbf{0} & \mathbf{0} & \mathbf{0} & \mathbf{0} & \mathbf{0} \\ \mathbf{0} & \mathbf{r}_{\sigma_y}^T & \mathbf{0} & \mathbf{0} & \mathbf{0} & \mathbf{0} \\ \mathbf{0} & \mathbf{0} & \mathbf{r}_{\sigma_z}^T & \mathbf{0} & \mathbf{0} & \mathbf{0} \\ \mathbf{0} & \mathbf{0} & \mathbf{0} & \mathbf{r}_{\tau_{xy}}^T & \mathbf{0} & \mathbf{0} \\ \mathbf{0} & \mathbf{0} & \mathbf{0} & \mathbf{0} & \mathbf{r}_{\tau_{xz}}^T & \mathbf{0} \\ \mathbf{0} & \mathbf{0} & \mathbf{0} & \mathbf{0} & \mathbf{0} & \mathbf{r}_{\tau_{yz}}^T \end{bmatrix} \begin{Bmatrix} \hat{\boldsymbol{\sigma}}_x \\ \hat{\boldsymbol{\sigma}}_y \\ \hat{\boldsymbol{\sigma}}_z \\ \hat{\boldsymbol{\tau}}_{xy} \\ \hat{\boldsymbol{\tau}}_{xz} \\ \hat{\boldsymbol{\tau}}_{yz} \end{Bmatrix} = \mathbf{R}_\sigma \hat{\boldsymbol{\sigma}} \quad (6)$$

In the same way we define the virtual field approximations:

$$\delta \mathbf{s} := \mathbf{R}_s \delta \hat{\mathbf{s}}; \quad \delta \boldsymbol{\sigma} := \mathbf{R}_\sigma \delta \hat{\boldsymbol{\sigma}}$$

According to the engineering notations just introduced, we re-define the differential operator and the normal unit vector product as follows:

Tensor notation	Engineering notation	
$\nabla \cdot \boldsymbol{\sigma}$	$\equiv$	$\left( \frac{\partial}{\partial x} \mathbf{E}_1 + \frac{\partial}{\partial y} \mathbf{E}_2 + \frac{\partial}{\partial z} \mathbf{E}_3 \right) \mathbf{R}_\sigma \hat{\boldsymbol{\sigma}}$
$\boldsymbol{\sigma} \cdot \mathbf{n}$	$\equiv$	$(n_x \mathbf{E}_1 + n_y \mathbf{E}_2 + n_z \mathbf{E}_3) \mathbf{R}_\sigma \hat{\boldsymbol{\sigma}}$

$$\quad (7)$$

$$\quad (8)$$

where products between partial derivatives and boolean matrices  $\mathbf{E}_i$ ,  $i = 1, 2, 3$  must be intended as scalar-matrix products, whereas differential operators are applied to stress approximations  $\mathbf{R}_\sigma \hat{\boldsymbol{\sigma}}$ . The boolean matrices  $\mathbf{E}_i$ ,  $i = 1, 2, 3$ , are defined as follows:

$$\begin{aligned} \mathbf{E}_1 &:= \begin{bmatrix} 1 & 0 & 0 & 0 & 0 & 0 \\ 0 & 0 & 0 & 1 & 0 & 0 \\ 0 & 0 & 0 & 0 & 1 & 0 \end{bmatrix} \\ \mathbf{E}_2 &:= \begin{bmatrix} 0 & 0 & 0 & 1 & 0 & 0 \\ 0 & 1 & 0 & 0 & 0 & 0 \\ 0 & 0 & 0 & 0 & 0 & 1 \end{bmatrix} \\ \mathbf{E}_3 &:= \begin{bmatrix} 0 & 0 & 0 & 0 & 1 & 0 \\ 0 & 0 & 0 & 0 & 0 & 1 \\ 0 & 0 & 1 & 0 & 0 & 0 \end{bmatrix} \end{aligned} \quad (9)$$

In Section 2, we denoted with  $\mathbf{D}^{-1}$  the fourth order, linear, elastic, isotropic tensor, while from now on, with a small abuse, we use the same notation to indicate the corresponding square matrix obtained following the

engineering notation. Therefore, we have:

$$\mathbf{D}^{-1} := \frac{1}{E} \begin{bmatrix} 1 & -\nu & -\nu & 0 & 0 & 0 \\ -\nu & 1 & -\nu & 0 & 0 & 0 \\ -\nu & -\nu & 1 & 0 & 0 & 0 \\ 0 & 0 & 0 & 2(1+\nu) & 0 & 0 \\ 0 & 0 & 0 & 0 & 2(1+\nu) & 0 \\ 0 & 0 & 0 & 0 & 0 & 2(1+\nu) \end{bmatrix} \quad (10)$$

Due to assumption (4), computation of partial derivatives is straightforward:

$$\begin{aligned} \frac{\partial}{\partial x} \gamma &= \mathbf{r}_\gamma^T \frac{d}{dx} \hat{\boldsymbol{\gamma}} = \mathbf{r}_\gamma^T \hat{\boldsymbol{\gamma}}' \\ \frac{\partial}{\partial y} \gamma &= \frac{\partial}{\partial y} \mathbf{r}_\gamma^T \hat{\boldsymbol{\gamma}} = \mathbf{r}_{\gamma,y}^T \hat{\boldsymbol{\gamma}}; \quad \frac{\partial}{\partial z} \gamma = \frac{\partial}{\partial z} \mathbf{r}_\gamma^T \hat{\boldsymbol{\gamma}} = \mathbf{r}_{\gamma,z}^T \hat{\boldsymbol{\gamma}} \end{aligned} \quad (11)$$

where the prime means the derivative along  $x$ ,  $(\cdot)_{,y}$  and  $(\cdot)_{,z}$  mean derivatives along  $y$  and  $z$ , respectively.

### 3.2. Model formulation

In the following we assume that  $\partial\Omega_s = A_0$ ,  $\partial\Omega_t = A_l \cup L$ , and the lateral surface is unloaded, i.e.:  $\mathbf{t}|_L = \mathbf{0}$ . The unloaded lateral surface is an usual assumption in beam modelling. However, we notice that the model derivation can be performed taking into account arbitrary load conditions as well.

In order to strongly satisfy the boundary equilibrium, according to the definition of  $S_t$ , see (2), we assume that the external traction  $\mathbf{t}|_{A_l}$  can be exactly represented using the profiles  $\mathbf{R}_\sigma$ . This means that there exist suitable vectors  $\hat{\mathbf{t}}_x$ ,  $\hat{\mathbf{t}}_y$ , and  $\hat{\mathbf{t}}_z$  such that:

$$\mathbf{t}|_{A_l} = \begin{Bmatrix} \mathbf{r}_{\sigma_x}^T \hat{\mathbf{t}}_x \\ \mathbf{r}_{\sigma_y}^T \hat{\mathbf{t}}_y \\ \mathbf{r}_{\sigma_z}^T \hat{\mathbf{t}}_z \end{Bmatrix} \quad (12)$$

Since  $\mathbf{n}|_{A_l} = (1, 0, 0)^T$ , Definition (8) becomes  $\boldsymbol{\sigma} \cdot \mathbf{n}|_{A_l} = \mathbf{E}_1 \mathbf{R}_\sigma \hat{\boldsymbol{\sigma}}(\bar{l})$  and the essential boundary condition  $\boldsymbol{\sigma} \cdot \mathbf{n}|_{A_l} = \mathbf{t}|_{A_l}$  can be expressed as follows:

$$\begin{Bmatrix} \hat{\boldsymbol{\sigma}}_x(\bar{l}) \\ \hat{\boldsymbol{\tau}}_{xy}(\bar{l}) \\ \hat{\boldsymbol{\tau}}_{xz}(\bar{l}) \end{Bmatrix} = \begin{Bmatrix} \hat{\mathbf{t}}_x \\ \hat{\mathbf{t}}_y \\ \hat{\mathbf{t}}_z \end{Bmatrix} \quad (13)$$

Introducing the engineering notation and the approximations defined in section 3.1, variational problem (3) becomes:

$$\begin{aligned} \delta J_{HR} &= - \int_{\Omega} \delta \hat{\mathbf{s}}^T \mathbf{R}_s^T \left[ \left( \frac{d}{dx} \mathbf{E}_1 + \frac{\partial}{\partial y} \mathbf{E}_2 + \frac{\partial}{\partial z} \mathbf{E}_3 \right) \mathbf{R}_\sigma \hat{\boldsymbol{\sigma}} \right] d\Omega \\ &\quad - \int_{\Omega} \left[ \left( \frac{d}{dx} \mathbf{E}_1 + \frac{\partial}{\partial y} \mathbf{E}_2 + \frac{\partial}{\partial z} \mathbf{E}_3 \right) \mathbf{R}_\sigma \delta \hat{\boldsymbol{\sigma}} \right]^T \mathbf{R}_s \hat{\mathbf{s}} d\Omega \\ &\quad - \int_{\Omega} \delta \hat{\boldsymbol{\sigma}}^T \mathbf{R}_\sigma^T \mathbf{D}^{-1} \mathbf{R}_\sigma \hat{\boldsymbol{\sigma}} d\Omega - \int_{\Omega} \delta \hat{\mathbf{s}}^T \mathbf{R}_s^T \mathbf{f} d\Omega \\ &\quad + \int_{\partial\Omega_s} [(n_x \mathbf{E}_1 + n_y \mathbf{E}_2 + n_z \mathbf{E}_3) \mathbf{R}_\sigma \delta \hat{\boldsymbol{\sigma}}]^T \bar{\boldsymbol{\tau}} dA = 0 \end{aligned} \quad (14)$$

Expanding products, introducing the derivative notation (11), and recalling that  $\partial\Omega_s = A_0$ , Equation (14) becomes:

$$\begin{aligned} \delta J_{HR} = & - \int_{\Omega} \left( \delta \hat{\mathbf{s}}^T \mathbf{R}_s^T \mathbf{E}_1 \mathbf{R}_{\sigma} \hat{\boldsymbol{\sigma}}' + \delta \hat{\mathbf{s}}^T \mathbf{R}_s^T \mathbf{E}_2 \mathbf{R}_{\sigma,y} \hat{\boldsymbol{\sigma}} \right. \\ & + \delta \hat{\mathbf{s}}^T \mathbf{R}_s^T \mathbf{E}_3 \mathbf{R}_{\sigma,z} \hat{\boldsymbol{\sigma}} + \delta \hat{\boldsymbol{\sigma}}'^T \mathbf{R}_{\sigma}^T \mathbf{E}_1^T \mathbf{R}_s \hat{\mathbf{s}} \\ & + \delta \hat{\boldsymbol{\sigma}}'^T \mathbf{R}_{\sigma,y}^T \mathbf{E}_2^T \mathbf{R}_s \hat{\mathbf{s}} + \delta \hat{\boldsymbol{\sigma}}'^T \mathbf{R}_{\sigma,z}^T \mathbf{E}_3^T \mathbf{R}_s \hat{\mathbf{s}} \\ & \left. + \delta \hat{\boldsymbol{\sigma}}^T \mathbf{R}_{\sigma}^T \mathbf{D}^{-1} \mathbf{R}_{\sigma} \hat{\boldsymbol{\sigma}} + \delta \hat{\mathbf{s}}^T \mathbf{R}_s^T \mathbf{f} \right) d\Omega \\ & - \int_{A_0} \delta \hat{\boldsymbol{\sigma}}^T \mathbf{R}_{\sigma}^T \mathbf{E}_1^T \bar{\mathbf{s}} dA = 0 \end{aligned} \quad (15)$$

Splitting the integral on the domain  $\Omega$  into an integral along the axis  $l$  and an integral on the cross section  $A$ , Equation (15) becomes:

$$\begin{aligned} \delta J_{HR} = & - \int_l \left( \delta \hat{\mathbf{s}}^T \mathbf{G}_{s\sigma} \hat{\boldsymbol{\sigma}}' + \delta \hat{\mathbf{s}}^T \mathbf{H}_{s\sigma} \hat{\boldsymbol{\sigma}} + \delta \hat{\boldsymbol{\sigma}}'^T \mathbf{G}_{\sigma s} \hat{\mathbf{s}} \right. \\ & \left. + \delta \hat{\boldsymbol{\sigma}}^T \mathbf{H}_{\sigma s} \hat{\mathbf{s}} + \delta \hat{\boldsymbol{\sigma}}^T \mathbf{H}_{\sigma\sigma} \hat{\boldsymbol{\sigma}} + \delta \hat{\mathbf{s}}^T \mathbf{F} \right) dx \\ & - \delta \hat{\boldsymbol{\sigma}}^T \bar{\mathbf{S}} = 0 \end{aligned} \quad (16)$$

where

$$\begin{aligned} \mathbf{H}_{s\sigma} & := \mathbf{H}_{\sigma s}^T = \int_A \left( \mathbf{R}_s^T \mathbf{E}_2 \mathbf{R}_{\sigma,y} + \mathbf{R}_s^T \mathbf{E}_3 \mathbf{R}_{\sigma,z} \right) dA \\ \mathbf{H}_{\sigma\sigma} & := \int_A \mathbf{R}_{\sigma}^T \mathbf{D}^{-1} \mathbf{R}_{\sigma} dA \\ \mathbf{G}_{s\sigma} = \mathbf{G}_{\sigma s}^T & := \int_A \mathbf{R}_s^T \mathbf{E}_1 \mathbf{R}_{\sigma} dA \\ \mathbf{F} & := \int_A \mathbf{R}_s^T \mathbf{f} dA; \quad \bar{\mathbf{S}} = \int_{A_0} \mathbf{R}_{\sigma}^T \mathbf{E}_1 \bar{\mathbf{s}} dA \end{aligned} \quad (17)$$

Equation (16) represents the weak formulation of the beam model: the integrals are defined only along the beam axis, whereas the cross-section integrals become coefficient matrices.

To obtain the corresponding strong formulation, i.e. the associated ODE system, we need to integrate by parts the third term of Equation (16):

$$- \int_l \delta \hat{\boldsymbol{\sigma}}'^T \mathbf{G}_{\sigma s} \hat{\mathbf{s}} dx = - \delta \hat{\boldsymbol{\sigma}}^T \mathbf{G}_{\sigma s} \hat{\mathbf{s}} \Big|_{x=0}^{x=l} + \int_l \delta \hat{\boldsymbol{\sigma}}^T \mathbf{G}_{\sigma s} \hat{\mathbf{s}}' dx \quad (18)$$

Substituting Equation (18) in Equation (16), recalling that  $\delta \hat{\boldsymbol{\sigma}}(\bar{l}) = \mathbf{0}$ , and collecting the unknowns in a vector, we obtain:

$$\begin{aligned} \int_l \left[ \delta \hat{\mathbf{s}}^T; \delta \hat{\boldsymbol{\sigma}}^T \right] \left( \mathbf{G} \begin{Bmatrix} \hat{\mathbf{s}}' \\ \hat{\boldsymbol{\sigma}}' \end{Bmatrix} + \mathbf{H} \begin{Bmatrix} \hat{\mathbf{s}} \\ \hat{\boldsymbol{\sigma}} \end{Bmatrix} - \begin{Bmatrix} \mathbf{F} \\ \mathbf{0} \end{Bmatrix} \right) dx \\ - \delta \hat{\boldsymbol{\sigma}}^T (\bar{\mathbf{S}} - \mathbf{G}_{\sigma s} \hat{\mathbf{s}}) = 0 \end{aligned} \quad (19)$$

where

$$\mathbf{G} := \begin{bmatrix} \mathbf{0} & -\mathbf{G}_{s\sigma} \\ \mathbf{G}_{\sigma s} & \mathbf{0} \end{bmatrix} \quad \mathbf{H} := \begin{bmatrix} \mathbf{0} & -\mathbf{H}_{s\sigma} \\ -\mathbf{H}_{\sigma s} & -\mathbf{H}_{\sigma\sigma} \end{bmatrix} \quad (20)$$

Since Equation (19) needs to be satisfied for all the possible virtual fields, we obtain the following ODE,

equipped with the essential boundary condition (13).

$$\begin{cases} \mathbf{G} \begin{Bmatrix} \hat{\mathbf{s}}' \\ \hat{\boldsymbol{\sigma}}' \end{Bmatrix} + \mathbf{H} \begin{Bmatrix} \hat{\mathbf{s}} \\ \hat{\boldsymbol{\sigma}} \end{Bmatrix} = \begin{Bmatrix} \mathbf{F} \\ \mathbf{0} \end{Bmatrix} & \text{in } l \\ \mathbf{G}_{\sigma_s} \hat{\mathbf{s}} = \bar{\mathbf{S}} & \text{at } x = 0 \\ \hat{\boldsymbol{\sigma}}_x = \hat{\mathbf{t}}_x & \text{at } x = \bar{l} \\ \hat{\boldsymbol{\tau}}_{xy} = \hat{\mathbf{t}}_y & \text{at } x = \bar{l} \\ \hat{\boldsymbol{\tau}}_{xz} = \hat{\mathbf{t}}_z & \text{at } x = \bar{l} \end{cases} \quad (21)$$

We notice that, since  $\mathbf{H}$  contains only  $y$  and  $z$  derivatives, it governs a generalized plane strain problem defined in the cross section. Furthermore, looking at the definition of  $\mathbf{G}$  (see (20)–(17)) and at the definition of the boolean matrix  $\mathbf{E}_1$  (see (9)), we observe that all the coefficients multiplying  $\hat{\boldsymbol{\sigma}}'_y$ ,  $\hat{\boldsymbol{\sigma}}'_z$ , and  $\hat{\boldsymbol{\tau}}'_{yz}$  vanish. As a consequence, we conclude that the beam model (21) is an algebraic-differential problem where at least  $\hat{\boldsymbol{\sigma}}_y$ ,  $\hat{\boldsymbol{\sigma}}_z$ , and  $\hat{\boldsymbol{\tau}}_{yz}$  are determined through purely algebraic equations.

### 3.3. Cross-section shape functions definition

Due to the domain definition (1) we can represent the stress tensor as follows:

$$\boldsymbol{\sigma} := \begin{bmatrix} \sigma_l & \boldsymbol{\tau}_{lA} \\ \boldsymbol{\tau}_{Al} & \boldsymbol{\sigma}_A \end{bmatrix} \quad (22)$$

where

$$\sigma_l := \sigma_{xx}; \quad \boldsymbol{\tau}_{lA} = \boldsymbol{\tau}_{Al}^T := [\tau_{xy}; \tau_{xz}]; \quad \boldsymbol{\sigma}_A := \begin{bmatrix} \sigma_{yy} & \tau_{yz} \\ \tau_{zy} & \sigma_{zz} \end{bmatrix}$$

Accordingly, we represent the divergence operator as follows:

$$\nabla := \left\{ \begin{array}{c} \frac{\partial}{\partial x} \\ \nabla_A \end{array} \right\} \quad \text{where} \quad \nabla_A := \left\{ \begin{array}{c} \frac{\partial}{\partial y} \\ \frac{\partial}{\partial z} \end{array} \right\} \quad (23)$$

We first recall that the space definition (2) requires in particular  $\boldsymbol{\sigma} \in H(\text{div}, \Omega)$ . Therefore, we must choose  $\boldsymbol{\sigma}$  such that  $(\nabla \cdot \boldsymbol{\sigma}) \in L^2(\Omega)$ , i.e.:

$$\nabla \cdot \boldsymbol{\sigma} = \left\{ \begin{array}{c} \frac{\partial}{\partial x} \sigma_l + \nabla_A \cdot \boldsymbol{\tau}_{lA} \\ \frac{\partial}{\partial x} \boldsymbol{\tau}_{Al} + \nabla_A \cdot \boldsymbol{\sigma}_A \end{array} \right\} \in L^2(\Omega) \quad (24)$$

Sufficient conditions that guarantee the satisfaction of (24) are the following:

$$\begin{aligned} \frac{\partial}{\partial x} \sigma_l &\in L^2(\Omega); & \nabla_A \cdot \boldsymbol{\tau}_{lA} &\in L^2(\Omega); \\ \frac{\partial}{\partial x} \boldsymbol{\tau}_{Al} &\in L^2(\Omega); & \nabla_A \cdot \boldsymbol{\sigma}_A &\in L^2(\Omega) \end{aligned} \quad (25)$$

In addition to Conditions (25), as suggested by Alessandrini et al. (1999), to ensure that the model is *well-posed*, one possible choice is to require the following condition:

$$\nabla \cdot S_0 = W \quad (26)$$

Given a generic cross-section geometry, it is not trivial to define cross-section shape functions that satisfy conditions (25) and (26). As a consequence, we start focusing on the simplest case, i.e. a beam with a rectangular cross-section:

$$A = \left\{ (y; z) \in \mathbb{R}^2 : y \in \left[ -\frac{h}{2}, \frac{h}{2} \right] \text{ and } z \in \left[ -\frac{b}{2}, \frac{b}{2} \right] \right\}$$

where  $h$  is the beam thickness and  $b$  is the beam depth. Due to the simplicity of the considered geometry, the cross-section shape functions can be defined as the tensor products of two *profile function vectors*  $\mathbf{p}_\gamma(y)$  and  $\mathbf{q}_\gamma(z)$ :

$$\mathbf{p}_\gamma : h \rightarrow \mathbb{R}^g; \quad \mathbf{q}_\gamma : b \rightarrow \mathbb{R}^k; \quad \mathbf{r}_\gamma^T := \text{vec}(\mathbf{p}_\gamma(y) \mathbf{q}_\gamma^T(z)) \quad (27)$$

where  $\text{vec}(\cdot)$  is the linear operator that re-arranges a tensor into a row vector. Obviously the  $g$  components of  $\mathbf{p}_\gamma$  and the  $k$  components of  $\mathbf{q}_\gamma$  are sets of linearly independent functions.

Due to the introduction of profile function definition (27), we can express Condition (26) as follows (cf. also (5) and (6)).

Given  $\hat{\mathbf{s}}$ , there exists  $\hat{\boldsymbol{\sigma}}$  such that:

$$\begin{aligned} \text{vec}(\mathbf{p}_{\sigma_x} \mathbf{q}_{\sigma_x}^T) \hat{\boldsymbol{\sigma}}'_x + \text{vec}(\mathbf{p}'_{\tau_{xy}} \mathbf{q}_{\tau_{xy}}^T) \hat{\boldsymbol{\tau}}_{xy} + \text{vec}(\mathbf{p}_{\tau_{xz}} \mathbf{q}'_{\tau_{xz}}{}^T) \hat{\boldsymbol{\tau}}_{xz} \\ = \text{vec}(\mathbf{p}_u \mathbf{q}_u^T) \hat{\mathbf{u}} \end{aligned} \quad (28)$$

$$\begin{aligned} \text{vec}(\mathbf{p}_{\tau_{xy}} \mathbf{q}_{\tau_{xy}}^T) \hat{\boldsymbol{\tau}}'_{xy} + \text{vec}(\mathbf{p}'_{\sigma_y} \mathbf{q}_{\sigma_y}^T) \hat{\boldsymbol{\sigma}}_y + \text{vec}(\mathbf{p}_{\tau_{yz}} \mathbf{q}'_{\tau_{yz}}{}^T) \hat{\boldsymbol{\tau}}_{yz} \\ = \text{vec}(\mathbf{p}_v \mathbf{q}_v^T) \hat{\mathbf{v}} \end{aligned} \quad (29)$$

$$\begin{aligned} \text{vec}(\mathbf{p}_{\tau_{xz}} \mathbf{q}'_{\tau_{xz}}{}^T) \hat{\boldsymbol{\tau}}'_{xz} + \text{vec}(\mathbf{p}'_{\tau_{yz}} \mathbf{q}_{\tau_{yz}}^T) \hat{\boldsymbol{\tau}}_{yz} + \text{vec}(\mathbf{p}_{\sigma_z} \mathbf{q}'_{\sigma_z}{}^T) \hat{\boldsymbol{\sigma}}_z \\ = \text{vec}(\mathbf{p}_w \mathbf{q}_w^T) \hat{\mathbf{w}}, \end{aligned} \quad (30)$$

and viceversa.

We consider complete polynomials as profile functions and we denote with  $\text{deg}(\cdot)$  their maximum degree. As a consequence, to satisfy Equations (28), (29), and (30) we enforce the following “natural” conditions:

$$\begin{aligned} \text{deg}(\mathbf{p}_{\sigma_x}) &= \text{deg}(\mathbf{p}_{\tau_{xy}}) - 1 = \text{deg}(\mathbf{p}_{\tau_{xz}}) = \text{deg}(\mathbf{p}_u) \\ \text{deg}(\mathbf{p}_{\tau_{xy}}) &= \text{deg}(\mathbf{p}_{\sigma_y}) - 1 = \text{deg}(\mathbf{p}_{\tau_{yz}}) = \text{deg}(\mathbf{p}_v) \\ \text{deg}(\mathbf{p}_{\tau_{xz}}) &= \text{deg}(\mathbf{p}_{\tau_{yz}}) - 1 = \text{deg}(\mathbf{p}_{\sigma_z}) = \text{deg}(\mathbf{p}_w) \\ \text{deg}(\mathbf{q}_{\sigma_x}) &= \text{deg}(\mathbf{q}_{\tau_{xy}}) = \text{deg}(\mathbf{q}_{\tau_{xz}}) - 1 = \text{deg}(\mathbf{q}_u) \\ \text{deg}(\mathbf{q}_{\tau_{xy}}) &= \text{deg}(\mathbf{q}_{\sigma_y}) = \text{deg}(\mathbf{q}_{\tau_{yz}}) - 1 = \text{deg}(\mathbf{q}_v) \\ \text{deg}(\mathbf{q}_{\tau_{xz}}) &= \text{deg}(\mathbf{q}_{\tau_{yz}}) = \text{deg}(\mathbf{q}_{\sigma_z}) - 1 = \text{deg}(\mathbf{q}_w) \end{aligned} \quad (31)$$

Table 1 displays the degree of profile functions  $\mathbf{p}_\gamma$  and  $\mathbf{q}_\gamma$ , assuming  $\text{deg}(\mathbf{p}_{\tau_{xy}}) = \text{deg}(\mathbf{q}_{\tau_{xz}}) = 2$  and imposing Equation (31).

As illustrated in Figure 3, we can define non-elementary cross-sections assembling elementary rectangular blocks that we call *fibers* and we suppose to be homogeneous. We construct the non elementary cross-section shape functions  $\mathbf{r}_\gamma$  considering the profile functions so far defined on each fiber, requiring the profile-function continuities specified in Table 1, and imposing the essential boundary condition  $\boldsymbol{\sigma} \cdot \mathbf{n}|_{\partial A} = \mathbf{0}$ . We specify that profile-function continuities are fixed in order to satisfy Condition (25).

### 3.4. Beam-model examples

In this sub-section we evaluate and discuss the solution of the beam model (21) for the homogeneous beam with square cross section depicted in Figure 4. We assume that the properties of the material are  $E =$

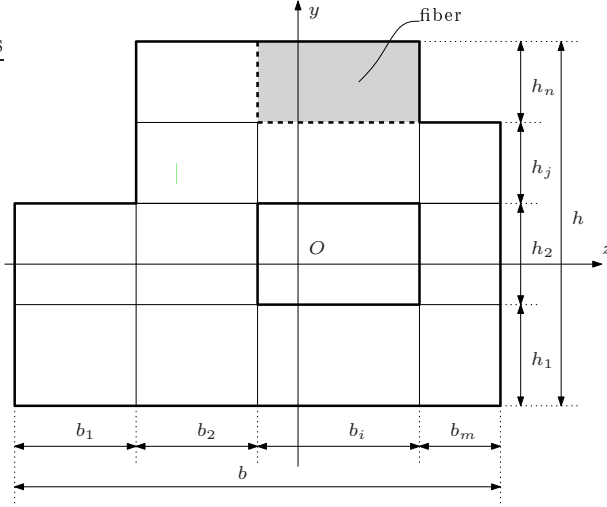


Figure 3: Non-elementary cross-section geometry definition, dimensions, and adopted notations.

Variable	$\deg(\mathbf{p}_\gamma)$	$y$ cont.	$\deg(\mathbf{q}_\gamma)$	$z$ cont.
$u$	1	$C^{-1}$	1	$C^{-1}$
$v$	2	$C^{-1}$	1	$C^{-1}$
$w$	1	$C^{-1}$	2	$C^{-1}$
$\sigma_x$	1	$C^{-1}$	1	$C^{-1}$
$\sigma_y$	3	$C^0$	1	$C^{-1}$
$\sigma_z$	1	$C^{-1}$	3	$C^0$
$\tau_{xy}$	2	$C^0$	1	$C^{-1}$
$\tau_{xz}$	1	$C^{-1}$	2	$C^0$
$\tau_{yz}$	2	$C^0$	2	$C^0$

Table 1: Degree and continuity of cross-section profile functions ( $C^{-1}$  means discontinuous function).

$10^5$  MPa and  $\nu = 0.25$  and, with respect to the notation introduced in Figure 3, the cross-section dimensions are  $h = b = 1$  mm. We model the physical problem using 2 cross-section discretization: the *one-fiber cross-section discretization*, depicted in Sub-figure 4(a), and the *two-fiber cross-section discretization*, depicted in Sub-figure 4(b); the aim of these modelling choices is to appreciate the effect of different discretization refinement.

In the following, the matrices  $\mathbf{G}$  and  $\mathbf{H}$  are evaluated through symbolic-calculus functions, whereas the further results are obtained using numerical-calculus functions, both implemented in MAPLE software.

#### 3.4.1. One-fiber cross-section

After imposition of the lateral free-traction boundary condition, the one-fiber cross-section beam has 33 unknowns. Since  $\text{rank}(\mathbf{G}) = 16$ , in the considered example we can distinguish between 16 unknowns that are solutions of a differential problem, and the remaining 17 that are algebraically determined by linear combination of the differential problem solutions. As already observed at the end of Sub-section 3.2, the 9  $\hat{\sigma}_y$ ,  $\hat{\sigma}_z$ , and  $\hat{\tau}_{yz}$  axial coefficient functions are among the ones algebraically determined. Moreover, looking at Equation (21) for the considered example, the boundary conditions are 16, since  $\text{rank}(\mathbf{G}_{\sigma_s}) = 8$  and the boundary equilibrium consists of 8 conditions. Therefore, the number of boundary conditions and the number of essential first order differential equations in (21) perfectly match.

As already explained in Auricchio et al. (2010), to construct the homogeneous solution of ODEs (21),

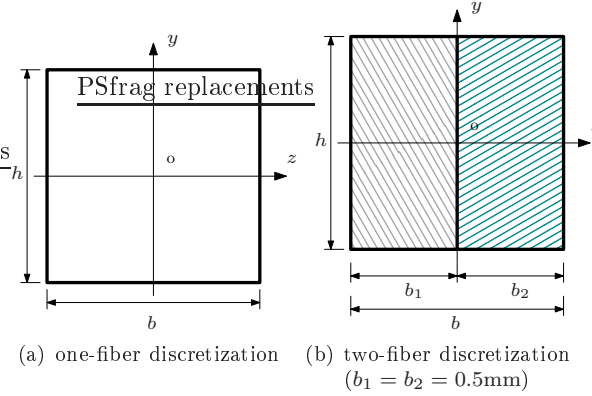


Figure 4: Homogeneous, square cross-section: dimensions and adopted discretization ( $h = b = 1\text{mm}$ ,  $E = 10^5\text{MPa}$ , and  $\nu = 0.25$ ).

we need the solution of the generalized eigenvalue problem:

$$\det(\lambda\mathbf{G} + \mathbf{H}) = 0 \quad (32)$$

where  $\lambda$  is the eigenvalue. For the case under investigation we obtain:

$$\lambda = \left\{ \begin{array}{c} \sim 0 \\ \pm 3.3652 \pm 1.1509i \end{array} \right\} \quad \begin{array}{l} [12] \\ [4] \end{array}$$

where the numbers in square brackets are the eigenvalue multiplicities (considering all the possible combination of sign of real and imaginary parts) and the notation  $\sim 0$  means that the eigenvalues vanish up to the machine precision.

#### 3.4.2. Two-fiber cross-section

After imposition of the lateral free-traction boundary condition, the two-fiber cross-section beam has 71 independent unknowns. Moreover,  $\text{rank}(\mathbf{G}) = 36$ . Hence, 36 unknowns are solution of a differential problem, whereas the remaining 35 are algebraically determined by linear combination of the differential problem solutions. Looking at Equation (21) for the considered example, the boundary conditions are 36, since  $\text{rank}(\mathbf{G}_{\sigma_s}) = 18$  and the boundary equilibrium consists of 18 conditions. Therefore, the number of boundary conditions and the number of essential first order differential equations in (21) perfectly match for this case, too.

In the two-fiber beam, the solution of the generalized eigenvalue problem (32) is:

$$\lambda = \left\{ \begin{array}{c} \sim 0 \\ \pm 11.786 \\ \pm 10.116 \\ \pm 10.022 \\ \pm 8.2174 \\ \pm 8.1037 \\ \pm 4.5891 \pm 1.2945i \\ \pm 5.6931 \pm 0.4331i \\ \pm 4.9317 \\ \pm 3.3520 \pm 1.1591i \end{array} \right\} \quad \begin{array}{l} [12] \\ [2] \\ [2] \\ [2] \\ [2] \\ [2] \\ [4] \\ [4] \\ [2] \\ [4] \end{array}$$

and it is going to be discussed in the next Sub-section.

### 3.4.3. Conclusions on beam models

We computed the solutions of the homogeneous problem associated to (21) for the beam models so far introduced, but we do not report them since their expressions are too long. However, the following remarks about the solution structure apply.

- Zero eigenvalues lead to polynomial terms, that correspond to the polynomial terms that appear also in the Saint-Venant solution. In particular, the 12 zero eigenvalues correspond to the 6 rigid body translations and to the 6 uniform deformations: extension, torque, two bendings, and two shears (associated with bendings).
- Non-zero, complex conjugate or real eigenvalues (generally represented as  $\pm a \pm ib$ ) lead to harmonic damped functions like  $C_j e^{\pm ax} \sin(bx + C_j)$ , that describe local effects near the boundaries, as it happens in other beam models, like Ladeveze and Simmonds (1998) and Allix and Duplex-Couderc (2010).

Similar conclusions was also reported in Lin et al. (2001) where, moreover, the authors specify that the real part of the eigenvalue defines the inverse decay length of the corresponding boundary effect. As a consequence, the smallest eigenvalue real-part provides an estimation of the length of the axis region where boundary effects are not negligible.

From the comparison between the one- and two-fiber cross-section beam models, it is possible to draw some additional observations.

- The number of eigenvalues corresponds exactly to the rank of  $\mathbf{G}$  matrix i.e. to the number of differential equations governing the problem.
- The number of null eigenvalues does not change. As a consequence, we may conclude that the polynomial terms in the solution are independent from the number of considered fibers.
- Instead, the number of non-zero eigenvalues increases with the fiber number. As a consequence, we may conclude that a finer discretization improves at least the accuracy of the description of local effects.
- The decay lengths of the two models are not so different (the smallest real part of eigenvalues are 3.3652 and 3.3520 for one- and two- fiber cross-sections, respectively). As a consequence, we may conclude that also the simplest model is effective in the evaluation of this parameter.
- In both models, the inverse of decay length ensures that the magnitude of damped functions is reduced of more than the 96% of its initial value, in a length of 1mm.

The independence of the polynomial solution with respect to the number of fibers suggests the idea that the modelling far from the extremal cross sections could be done by means of few global degrees of freedom, as in EB beam model. However, this idea will be the topic of future investigations.

## 4. FE derivation

The goal of this section is to obtain a displacement-based beam FE formulation. Accordingly, we introduce an approximation along the  $x$  direction, modify the beam-model weak formulation (16), and perform an integration along the axis. The procedure reduces the algebraic-differential equation system (21) to a pure algebraic equation system.

### 4.1. Axial approximation

We introduce the following approximation:

$$\hat{\boldsymbol{\gamma}}(x) \approx \mathbf{N}_\gamma(x) \tilde{\boldsymbol{\gamma}} \quad (33)$$

where

$$\mathbf{N}_\gamma = \begin{bmatrix} \mathbf{N}_{\gamma_1}^T(x) & \mathbf{0} & \cdots & \mathbf{0} \\ \mathbf{0} & \mathbf{N}_{\gamma_2}^T(x) & \cdots & \mathbf{0} \\ \vdots & \vdots & \ddots & \vdots \\ \mathbf{0} & \mathbf{0} & \cdots & \mathbf{N}_{\gamma_d}^T(x) \end{bmatrix}$$

$$\tilde{\boldsymbol{\gamma}} = \{\tilde{\boldsymbol{\gamma}}_1, \tilde{\boldsymbol{\gamma}}_2, \cdots, \tilde{\boldsymbol{\gamma}}_d\}^T$$

Accordingly, the  $i$ -th axial coefficient function  $\hat{\gamma}_i(x)$  is approximated as a linear combination of some assigned *axial shape functions*, stored in the vector  $\mathbf{N}_{\gamma_i} : l \rightarrow \mathbb{R}^t$ ; the *numerical coefficients* of the combination are collected in the vector  $\tilde{\boldsymbol{\gamma}}_i \in \mathbb{R}^t$ . In the following, we drop the explicit dependence of  $\mathbf{N}_\gamma$  on  $x$  for notational simplicity.

#### 4.2. FE formulation

In the following, we assume that the beam is clamped in  $A_0$ , i.e.  $\bar{\boldsymbol{\mathfrak{s}}} = \mathbf{0}$ . Starting from beam-model weak formulation (16), we integrate by parts with respect to the  $x$  direction both the first and the third terms obtaining the following, alternative beam-model weak formulation:

Find  $\hat{\boldsymbol{s}} \in \tilde{W}$  and  $\hat{\boldsymbol{\sigma}} \in \tilde{S}$  such that  $\forall \delta \hat{\boldsymbol{s}} \in \tilde{W}$  and  $\forall \delta \hat{\boldsymbol{\sigma}} \in \tilde{S}$

$$\begin{aligned} \delta J_{HR} = \int_l & (\delta \hat{\boldsymbol{s}}^T \mathbf{G}_{s\sigma} \hat{\boldsymbol{\sigma}} - \delta \hat{\boldsymbol{s}}^T \mathbf{H}_{s\sigma} \hat{\boldsymbol{\sigma}} + \delta \hat{\boldsymbol{\sigma}}^T \mathbf{G}_{\sigma s} \hat{\boldsymbol{s}}' \\ & - \delta \hat{\boldsymbol{\sigma}}^T \mathbf{H}_{\sigma s} \hat{\boldsymbol{s}} - \delta \hat{\boldsymbol{\sigma}}^T \mathbf{H}_{\sigma\sigma} \hat{\boldsymbol{\sigma}} - \delta \hat{\boldsymbol{s}}^T \mathbf{F}) dx \\ & - \delta \hat{\boldsymbol{s}}^T \mathbf{T} = 0 \end{aligned} \tag{34}$$

where  $\mathbf{T} := \int_{A_l} \mathbf{R}_s^T \mathbf{t} dA$ ,  $\tilde{W} := \{\hat{\boldsymbol{s}} \in H^1(l) : \hat{\boldsymbol{s}}|_{x=0} = \mathbf{0}\}$ , and  $\tilde{S} := L^2(l)$ . We recall that:

$$L^2(l) := \left\{ \hat{\boldsymbol{\sigma}} : \int_l \hat{\boldsymbol{\sigma}}^T \hat{\boldsymbol{\sigma}} dx < \infty \right\}$$

$$H^1(l) := \left\{ \hat{\boldsymbol{s}} : \hat{\boldsymbol{s}}, \hat{\boldsymbol{s}}' \in L^2(l) \right\}$$

The FE discretization of the model follows from the introduction of the axial shape function approximation (33) into the beam-model weak formulation (34):

$$\begin{aligned} \delta J_{HR} = \int_l & (\delta \tilde{\boldsymbol{s}}^T \mathbf{N}_s^T \mathbf{G}_{s\sigma} \mathbf{N}_\sigma \tilde{\boldsymbol{\sigma}} - \delta \tilde{\boldsymbol{s}}^T \mathbf{N}_s^T \mathbf{H}_{s\sigma} \mathbf{N}_\sigma \tilde{\boldsymbol{\sigma}} \\ & + \delta \tilde{\boldsymbol{\sigma}}^T \mathbf{N}_\sigma^T \mathbf{G}_{\sigma s} \mathbf{N}_s' \tilde{\boldsymbol{s}} - \delta \tilde{\boldsymbol{\sigma}}^T \mathbf{N}_\sigma^T \mathbf{H}_{\sigma s} \mathbf{N}_s \tilde{\boldsymbol{s}} \\ & - \delta \tilde{\boldsymbol{\sigma}}^T \mathbf{N}_\sigma^T \mathbf{H}_{\sigma\sigma} \mathbf{N}_\sigma \tilde{\boldsymbol{\sigma}} - \delta \tilde{\boldsymbol{s}}^T \mathbf{N}_s^T \mathbf{F}) dx \\ & - \delta \tilde{\boldsymbol{s}}^T \mathbf{N}_s^T \mathbf{T} = 0 \end{aligned} \tag{35}$$

Collecting unknown coefficients in a vector and requiring (35) to be satisfied for all possible virtual fields, we obtain the following algebraic equation system:

$$\begin{bmatrix} \mathbf{0} & \mathbf{K}_{s\sigma} \\ \mathbf{K}_{\sigma s} & \mathbf{K}_{\sigma\sigma} \end{bmatrix} \begin{Bmatrix} \tilde{\boldsymbol{s}} \\ \tilde{\boldsymbol{\sigma}} \end{Bmatrix} = \begin{Bmatrix} \tilde{\mathbf{T}} \\ \mathbf{0} \end{Bmatrix} \tag{36}$$

where

$$\mathbf{K}_{s\sigma} = \mathbf{K}_{\sigma s}^T := \int_l (\mathbf{N}_s^T \mathbf{G}_{s\sigma} \mathbf{N}_\sigma - \mathbf{N}_s^T \mathbf{H}_{s\sigma} \mathbf{N}_\sigma) dx$$

$$\mathbf{K}_{\sigma\sigma} := - \int_l \mathbf{N}_\sigma^T \mathbf{H}_{\sigma\sigma} \mathbf{N}_\sigma dx; \tilde{\mathbf{T}} := \int_l \mathbf{N}_s^T \mathbf{F} dx + \mathbf{N}_s^T|_{x=l} \mathbf{T}$$

We highlight the following remarks.

- Since  $\hat{\mathbf{s}} \in \widetilde{W}$ , the continuity of displacements along the beam axis is satisfied *a priori*, whereas axial equilibrium is *weakly* imposed through Equation (34).
- The weak formulation (34) is symmetric.

#### 4.3. Axial shape functions definition

In this sub-section we specify how to choose the FE approximation spaces. We first notice that, since  $\mathbf{s} \in H^1(l)$ , we need to impose axial continuity on displacements. Instead, since  $\boldsymbol{\sigma} \in L^2(l)$  stress components can be axial-discontinuous, and in general it is convenient that they are so. Furthermore, to properly balance the discrete spaces, it seems reasonable to choose  $\widetilde{W}$  and  $\widetilde{S}$  satisfying:  $\forall \hat{\boldsymbol{\sigma}} \in \widetilde{S}$  there exists  $\hat{\mathbf{s}} \in \widetilde{W}$  such that

$$\frac{d}{dx}\hat{\mathbf{s}} = \mathbf{E}_1\hat{\boldsymbol{\sigma}}; \quad \hat{\mathbf{s}} = \mathbf{E}_2\hat{\boldsymbol{\sigma}}; \quad \hat{\mathbf{s}} = \mathbf{E}_3\hat{\boldsymbol{\sigma}}, \quad (37)$$

and viceversa.

Accordingly, we require the following conditions on the axial shape functions:

$$\begin{aligned} \deg(\mathbf{N}_u) &= \deg(\mathbf{N}_{\sigma_x}) + 1 = \deg(\mathbf{N}_{\tau_{xy}}) = \deg(\mathbf{N}_{\tau_{xz}}) \\ \deg(\mathbf{N}_v) &= \deg(\mathbf{N}_{\tau_{xy}}) + 1 = \deg(\mathbf{N}_{\sigma_y}) = \deg(\mathbf{N}_{\tau_{yz}}) \\ \deg(\mathbf{N}_w) &= \deg(\mathbf{N}_{\tau_{xz}}) + 1 = \deg(\mathbf{N}_{\tau_{yz}}) = \deg(\mathbf{N}_{\sigma_z}) \end{aligned} \quad (38)$$

Assuming  $\deg(\mathbf{N}_v) = 3$  and imposing Equations (38), we determine the degree of axis shape functions  $\mathbf{N}_\gamma$ , summarized in Table 2 together with properties of profile vectors.

Variable	$\deg(\mathbf{p}_\gamma)$	$y$ cont.	$\deg(\mathbf{q}_\gamma)$	$z$ cont.	$\deg(\mathbf{N}_\gamma)$	$x$ cont.
$u$	1	$C^{-1}$	1	$C^{-1}$	2	$C^0$
$v$	2	$C^{-1}$	1	$C^{-1}$	3	$C^0$
$w$	1	$C^{-1}$	2	$C^{-1}$	3	$C^0$
$\sigma_x$	1	$C^{-1}$	1	$C^{-1}$	1	$C^{-1}$
$\sigma_y$	3	$C^0$	1	$C^{-1}$	3	$C^{-1}$
$\sigma_z$	1	$C^{-1}$	3	$C^0$	3	$C^{-1}$
$\tau_{xy}$	2	$C^0$	1	$C^{-1}$	2	$C^{-1}$
$\tau_{xz}$	1	$C^{-1}$	2	$C^0$	2	$C^{-1}$
$\tau_{yz}$	2	$C^0$	2	$C^0$	3	$C^{-1}$

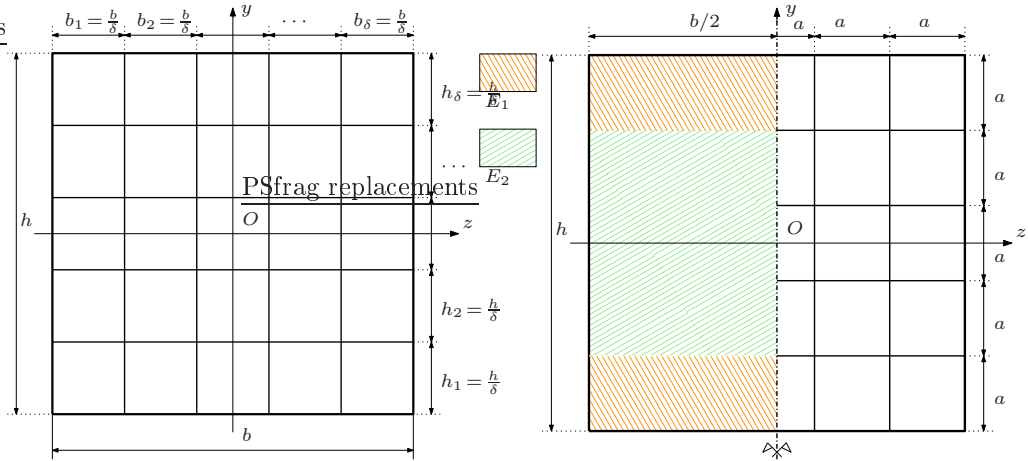
Table 2: Degree and continuity of cross-section profile functions and axis shape functions ( $C^{-1}$  means discontinuous function)

Looking at the properties of the axial shape functions summarized in Table 2, we notice that all stress components are discontinuous along the beam axis. Moreover, the matrix  $\mathbf{H}_{\sigma\sigma}$  (see (17) and (10)) is invertible. Therefore, it is possible to statically condense the stress variables out at the element level. This leads to a displacement-based-like formulation of the problem, thus significantly reducing the dimension of the global stiffness matrix and improving the FE algorithm efficiency.

## 5. Numerical results

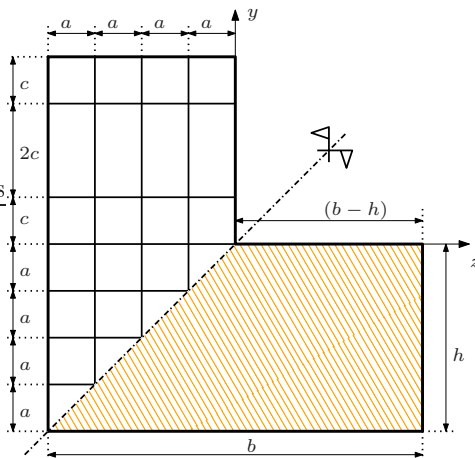
The goal of this section is to illustrate the capability of the beam model and FE introduced so far. Accordingly, we consider the problems listed below.

1. Homogeneous square cross-section beam, depicted in Figure 5(a).
2. Non-homogeneous square cross-section beam, depicted in Figure 5(b).
3. Homogeneous L-shape cross-section beam, depicted in Figure 5(c).



(a) non-homogeneous cross section: geometry and mesh definition (in the considered example  $h = b = 1\text{mm}$ ,  $\delta$  variable,  $E = 10^5\text{MPa}$ , and  $\nu = 0.25$ )

(b) non-homogeneous cross section: geometry and mesh definition (in the considered example  $h = b = 1\text{mm}$ ,  $a = 0.2\text{mm}$ ,  $E_1 = 10^5\text{MPa}$ ,  $E_2 = 10^3\text{MPa}$ , and  $\nu = 0.25$ )



(c) L-shape cross section: geometry and mesh definition (in the considered example  $b = 1\text{mm}$ ,  $h = 0.5\text{mm}$ ,  $a = c = 0.125\text{mm}$ ,  $E = 10^5\text{MPa}$ , and  $\nu = 0.25$ )

Figure 5: Cross-sections geometries and discretizations of the beams considered in Section 5.

We introduce the relative error definition for a generic variable  $\gamma$ :

$$e_{\gamma rel} := \frac{|\gamma - \gamma^{ref}|}{|\gamma^{ref}|} \quad (39)$$

where  $\gamma^{ref}$  is the reference solution, to be specified for each problem under investigation.

FE solutions considered in this section are evaluated through numerical-calculus functions implemented in MATLAB software, unless specified.

### 5.1. Homogeneous square cross-section beam

We consider the homogeneous beam with a square cross-section depicted in Figure 5(a) and we discuss the following aspects.

1. Displacement error and convergence of displacement solution.
2. Stress error.
3. Asymptotic behaviour.

We recall that, in FE derivation, the beam is assumed to be clamped at the initial cross-section ( $\partial\Omega_s = A_0$ ;  $\bar{\mathbf{s}} = \mathbf{0}$ ); moreover, we set  $\bar{l} = 10\text{mm}$ , vanishing volume load ( $\mathbf{f} = \mathbf{0}$ ), and a distributed shear load applied to the final cross section  $A_l$  ( $\mathbf{t}|_{A_l} = [0, -1, 0]^T$  MPa). In Figure 5(a), we define the parameter  $\delta$  that defines both the cross-section and the axial discretizations where the length of the  $k^{th}$  axis FE is defined as  $l_k := \bar{l} / (10 \cdot \delta)$ .

In the following, the acronym MB FE (Mixed Beam Finite Element) denotes the beam model FE discretization of Equation (36).

#### 5.1.1. Displacement error

We consider the  $y$ -oriented displacement component  $s_v$  (see Definition (5)) and we evaluate its mean value  $\bar{v}(\bar{l})$  on the final cross section  $A_l$ :

$$\bar{v}(\bar{l}) := \frac{\int_{A_l} \mathbf{r}_v^T \hat{\mathbf{v}}|_{x=\bar{l}} dydz}{\int_{A_l} dydz} \quad (40)$$

In order to discuss the displacement solution of the MB FE, we compare the solutions of the models listed in the following.

- The analytical solution of Euler-Bernoulli beam,
- The analytical solution of Timoshenko beam,
- The numerical solution of the MB FE evaluated considering two cases:
  - 1 fiber cross-section (i.e.  $\delta = 1$ ),
  - 25 fiber cross-section (i.e.  $\delta = 5$ ).
- 3D numerical solutions obtained using the software ABAQUS and with 3D trilinear bricks. The following uniform meshes are employed.
  - A uniform mesh of  $5 \times 5 \times 50$  elements.
  - A uniform mesh of  $10 \times 10 \times 100$  elements.
  - A fine and uniform mesh of  $50 \times 50 \times 500$  elements. This overkilled solution is used as the reference solution  $s_v^{ref}$ .

Beam model	$\bar{v}(10)$ mm	$e_{vrel}$
Euler-Bernoulli	$-4.000000 \cdot 10^{-2}$	$3.222 \cdot 10^{-3}$
Timoshenko	$-4.030000 \cdot 10^{-2}$	$4.254 \cdot 10^{-3}$
MB FE 1 fiber ( $\delta = 1$ )	$-4.022380 \cdot 10^{-2}$	$2.355 \cdot 10^{-3}$
MB FE 25 fiber ( $\delta = 5$ )	$-4.012917 \cdot 10^{-2}$	$0.003 \cdot 10^{-3}$
3D solution (mesh $5 \times 5 \times 50$ )	$-4.175198 \cdot 10^{-2}$	$40.437 \cdot 10^{-3}$
3D solution (mesh $10 \times 10 \times 100$ )	$-4.051178 \cdot 10^{-2}$	$9.531 \cdot 10^{-3}$
3D solution ( $v^{ref}$ )	$-4.012929 \cdot 10^{-2}$	-

Table 3: Mean value of final cross-section displacement  $\bar{v}(10)$  and the corresponding relative error for a cantilever ( $\bar{l} = 10\text{mm}$ ,  $b = h = 1\text{mm}$ ) evaluated using different beam models.

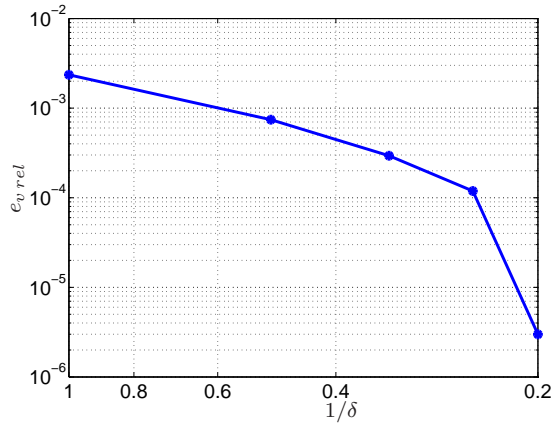


Figure 6: Relative error  $e_{vrel}$  plotted as function of the element size  $1/\delta$ .

In Table 3 we report the vertical-displacement mean-value  $\bar{v}(\bar{l})$  for the considered beam models and their relative errors. We notice that all the models, even the two simplest ones (i.e., the Euler-Bernoulli and the Timoshenko models) give a relative error below 5%. Furthermore, as expected, MB FE 25 fiber model provides the best solution, with a relative error close to  $10^{-6}$ , negligible in most practical applications. In addition, despite the coarse discretization in the modelling procedure, the MB FE 1 fiber relative error is of the order of 2%, better than both Euler-Bernoulli and Timoshenko beams.

In Figure 6 we plot the relative error  $e_{vrel}$  as function of the element size  $1/\delta$ . It is worth observing the monotonic behaviour and the high speed convergence.

### 5.1.2. Stress error

We focus our attention to the shear components  $\tau_{xy}$  and  $\tau_{xz}$  since they have non-trivial distributions. In the following, the numerical results refer to the 25 fiber discretization.

Figures 7(a) and 7(b) report the shear axial coefficient functions  $\hat{\tau}_{xy}$  and  $\hat{\tau}_{xz}$  respectively. We remark that they show damped oscillations near the initial and final cross sections, while they are approximately constant otherwise. We notice that this numerical behaviour is consistent with the ODEs homogeneous solutions discussed in Section 3.4.

Moreover, the oscillations rapidly decay in an axial region whose length is of the order of magnitude of the cross-section edge, in accordance with the solution provided by the Saint-Venant principle.

Figures 8(a) and 8(b) report the cross-section distribution of shear components  $\tau_{xy}(5, y, z)$  and  $\tau_{xz}(5, y, z)$  respectively. We consider the cross section at  $x = 5\text{mm}$  in order to exclude boundary effects. It is worth noticing that the cross-section shear component  $\tau_{xy}$  has a parabolic distribution along  $y$ . Moreover,  $\tau_{xy}$  is not constant along  $z$ , and the shear component  $\tau_{xz}$  displays a non vanishing distribution in the cross section.

These latter results provide a shear stress evaluation which is better than the one given by the simplified Jourawsky theory (e.g. Hjelmstad (2005)), usually adopted in connection with classical beam models.

Figures 8(c) and 8(d) report the cross-section error distributions  $|\tau_{xy}(5, y, z) - \tau_{xy}^{ref}(5, y, z)|$  and  $|\tau_{xz}(5, y, z) - \tau_{xz}^{ref}(5, y, z)|$  where  $\tau_{xy}^{ref}(5, y, z)$  and  $\tau_{xz}^{ref}(5, y, z)$  are reference solutions obtained using the results detailed in Timoshenko and Goodier (1951)[Chap. 12]. It is interesting to note that the numerical solution appears to be generally accurate. However, the error is higher close to the cross section edges.

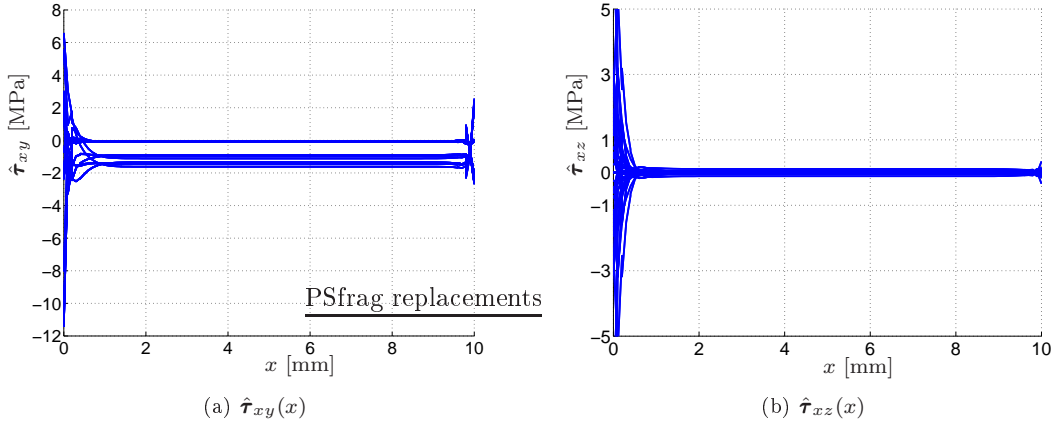


Figure 7: Shear axial coefficient functions  $\hat{\tau}_{xy}(x)$  and  $\hat{\tau}_{xz}(x)$  for the case of homogeneous and square cross section.

### 5.1.3. Asymptotic analysis

In this sub-section, we investigate the beam model behaviour as the cross-section size tends to zero. It can be shown that the 3D beam solution converges to the EB solution, after a suitable scaling of the loads (see Ciarlet (1997), for instance). In this section we numerically verify that, decreasing the cross-section size, the MB FE solution converges to the EB solution, thus ensuring the asymptotic consistency of the proposed beam model.

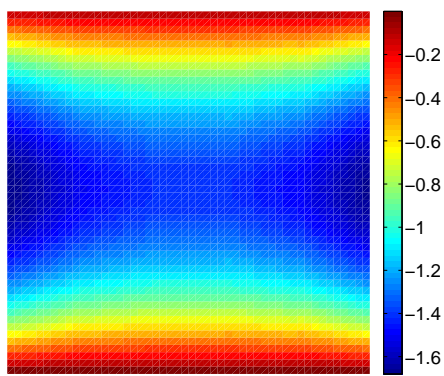
We consider a beam with length and boundary conditions introduced in Section 5.1, and using a single square fiber to discretize the cross section. We use uniform meshes along the beam axis, and different decreasing values of the cross section size  $h$ . We implement the MB FE using numerical functions available in MAPLE software. In particular, we exploit the capability of the software to use an arbitrary number of digits during numerical calculation. Since we are interested in the asymptotic behaviour, the EB beam solution  $\bar{v}^{ref}(\bar{l})$  is assumed as reference solution.

In Figure 9 we plot the relative error  $e_{vrel}$  evaluated at different ratios  $h/\bar{l}$ , for different axial meshes (4 and 50 elements, respectively), and for different machine precisions (16 and 30 digits, respectively). We notice that bad solutions are computed when using 16 digits and for very small ratios  $h/\bar{l}$ , independently of the number of elements. However, satisfactory results are obtained for slendernesses of practical engineering interest. On the contrary, raising to 30 digits, the computed solutions display the correct behaviour. We remark that the plateau regions for 4el(30dig) and 50el(30dig) in Figure 9 correspond to the error due to the axial discretization, which dominates the total error in the asymptotic regime ( $h/\bar{l} \ll 1$ ).

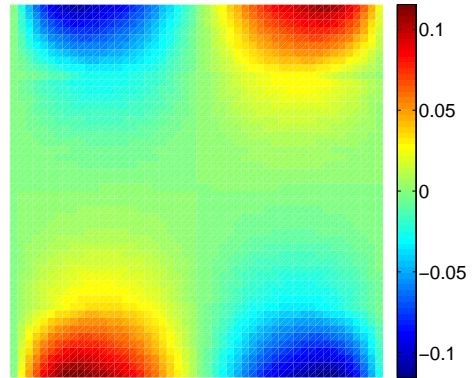
In Figure 10 we show the relative error of the single fiber MB FE, considering different ratios  $h/\bar{l}$  and varying the number of elements in the axial direction. The plot confirms the convergence of the solution, independently of the ratio  $h/\bar{l}$  when 30 digits are employed. As already noticed, a degeneracy in the convergence behaviour is experienced for very small  $h/\bar{l}$  and 16 digit precision.

### 5.1.4. Computational costs

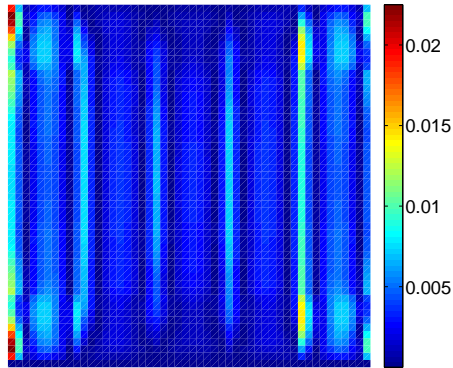
In this subsection we give some information about the computational performance of the proposed method, comparing the numerical costs with the costs of a 3D displacement based analysis of the homoge-



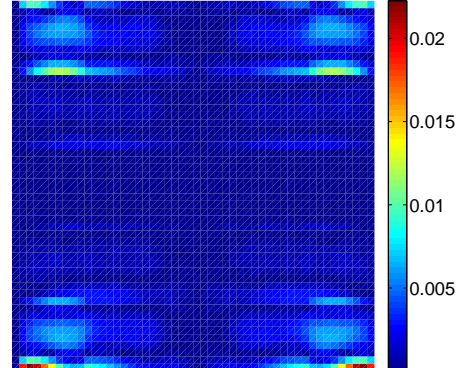
(a)  $\tau_{xy}(5, y, z)$



(b)  $\tau_{xz}(5, y, z)$



(c) shear error  $|\tau_{xy}(5, y, z) - \tau_{xy}^{ref}(5, y, z)|$



(d) shear error  $|\tau_{xz}(5, y, z) - \tau_{xz}^{ref}(5, y, z)|$

Figure 8: Shear cross-section distributions (8(a) and 8(b)) and cross-section error distributions (8(c) and 8(d)) for the case of homogeneous and square cross section.

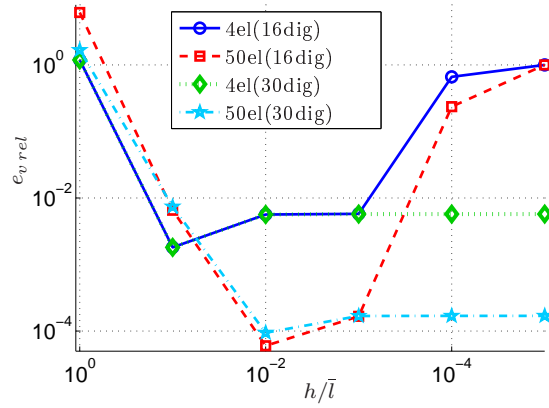


Figure 9: Relative asymptotic error.

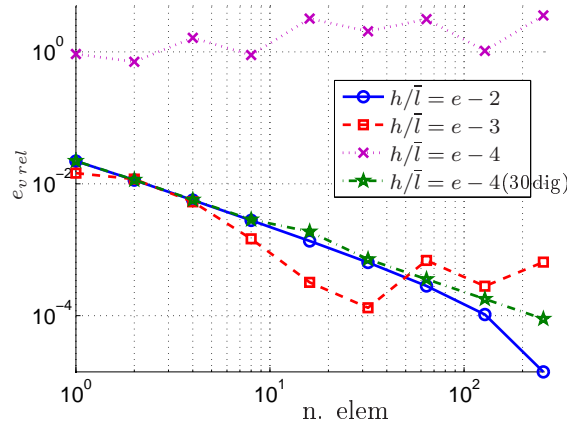


Figure 10: Relative error  $e_{v,rel}$  plotted as function of the number of elements for different ratios  $h/\bar{l}$

neous square cross-section beam.

The time elapsed to compute the solutions is not a fair criterion due to the use of different softwares and machines. Instead, in Table 4 we provide some information that may be used to compare the different approaches. We notice that, in all the considered cases, the global stiffness matrices governing the problem will be symmetric, sparse, and with a band structure.

The displacement relative error  $e_{v,rel}$  is the same as reported in Table 3 and it provides information about the solution accuracy. The estimation of the number of DOFs ( $\#$  DOFs) corresponds to the size of the global stiffness matrix. In particular, for the 1- and 5- fiber models,  $\#$  DOFs does not take into account the number of variables condensed out at the element level, since negligible with respect to number of global DOFs (e.g. in the 5 fibre model  $\sim 1.5 \cdot 10^3$  DOFs are condensed on each element). The number of non-vanishing entries in the global stiffness matrices ( $\#$  entries  $\neq 0$ ) is strictly related to the memory usage during computation. The fourth column of Table 4 reports an estimation of the band width. The fifth column reports an estimation of the number of flops necessary to LU-factorize the global stiffness matrix ( $\#$  flops), under the following assumptions: (i)  $\#$  DOFs  $\gg$  band-width and (ii) the computational cost of both the assembling procedure and the post-processing are negligible. As a consequence,  $\#$  flops is evaluated

Model	$\epsilon_{vrel}$	# DOFs	# entries $\neq 0$	band-width	# flops
MB FE 1 fiber ( $\delta = 1$ )	$2.355 \cdot 10^{-3}$	$1.60 \cdot 10^2$	$7.17 \cdot 10^3$	$3.30 \cdot 10^1$	$8.71 \cdot 10^4$
MB FE 25 fiber ( $\delta = 5$ )	$0.003 \cdot 10^{-3}$	$2.00 \cdot 10^4$	$2.37 \cdot 10^7$	$1.60 \cdot 10^3$	$2.57 \cdot 10^{10}$
3D solution (mesh $5 \times 5 \times 50$ )	$40.437 \cdot 10^{-3}$	$5.40 \cdot 10^3$	$4.37 \cdot 10^5$	$4.33 \cdot 10^2$	$5.05 \cdot 10^8$
3D solution (mesh $10 \times 10 \times 100$ )	$9.531 \cdot 10^{-3}$	$3.63 \cdot 10^4$	$2.94 \cdot 10^6$	$1.45 \cdot 10^3$	$3.83 \cdot 10^{10}$
3D solution (mesh $50 \times 50 \times 500$ )	-	$3.90 \cdot 10^6$	$3.16 \cdot 10^8$	$3.12 \cdot 10^4$	$1.90 \cdot 10^{15}$

Table 4: Final cross-section displacement relative error, number of DOFs used in the analysis (# DOFs), number of global stiffness-matrix entries different from zero (# entries  $\neq 0$ ), band width of the global stiffness matrix (band-width), and estimation of the number of flops necessary to factorize the global stiffness matrix (# flops) for a cantilever ( $\bar{l} = 10\text{mm}$ ,  $b = h = 1\text{mm}$ ) evaluated using different beam models.

through the following equation (see Quarteroni et al., 2007):

$$\# \text{ flops} = \frac{\# \text{ DOFs} \cdot (\text{band-width})^2}{2} \quad (41)$$

We highlight that the MB FE 25 fiber and the 3D solution (mesh  $10 \times 10 \times 100$ ) require comaprable # flops. Nevertheless, the former model provides a solution with a relative error that is 3 order of magnitude smaller than the latter. The obtained results, even if non exhaustive, lead us to conclude that the proposed method has interesting numerical performances with respect to the standard 3D analysis.

#### 5.1.5. Conclusions on the beam model and the corresponding FE scheme

Looking at all the analyses performed in this section, we may remark what follows.

- As illustrated in Subsection 5.1.1, the MB and the corresponding FE scheme can capture the real displacement better than the most popular beam models (EB and Timoshenko models).
- As illustrated in Subsection 5.1.2, the proposed beam model has a significant accuracy in the stress description.
- As illustrated in Subsection 5.1.3, the asymptotic behaviour, for reasonable ratios  $h/\bar{l}$ , is correct. Nevertheless, we note that the MB FE scheme may exhibits troubles for extremely small ratios  $h/\bar{l}$ .
- As illustrated in Subsection 5.1.4, the MB FE is numerically competitive with respect to standard methods.

#### 5.2. Non homogeneous cross-section beam (soft core beam)

In this subsection we consider a beam with the non-homogeneous square cross-section depicted in Figure 5(b), and modeled through 25 equal fibers. We assume the boundary conditions of the example in Section 5.1. Furthermore, we set  $\bar{l} = 20\text{mm}$ ,  $E_1 = 10^5\text{MPa}$ ,  $E_2 = 10^3\text{MPa}$ , and  $\nu = 0.25$  everywhere in the cross section. Along the beam axis we use a non-uniform 8 element meshes, whose nodal coordinates are collected in the following vector:  $[0; 1; 2; 3; 10; 17; 18; 19; 20]$ . We plot the stress distribution in the cross section  $x = 10\text{mm}$ . The numerical results are reported in Figure 11.

Consistently with the Saint-Venant principle, the stress components  $\sigma_{yy}$ ,  $\sigma_{zz}$  and  $\tau_{yz}$  are negligible. Moreover, due to the large ratio between the two Young's moduli, stress distributions within the core appear always extremely regular and flat.

In this example the non uniform distribution of shear component  $\tau_{xy}$  along  $z$ -direction is less evident than in the case of homogeneous beam. The ratio between the maximum values of the shears  $\tau_{xy}$  and  $\tau_{xz}$ , is close to 10, which confirms, once again, that  $\tau_{xz}$  should not be neglected. In order to validate the results, we compute a 3D numerical solution using the ABAQUS software and a homogeneous mesh of 40 brick elements. In Table 5 we report the minimum and the maximum values of the cross-section stress distribution evaluated on the cross-section  $x = 10\text{mm}$ . From the comparison of the two methods it is possible to appreciate the substantial agreement of the results. We notice that the high value of the  $\sigma_y$ ,  $\sigma_z$ , and  $\tau_{yz}$  in ABAQUS min and max evaluation depends on some localized instabilities that occur in numerical evaluation of stress.

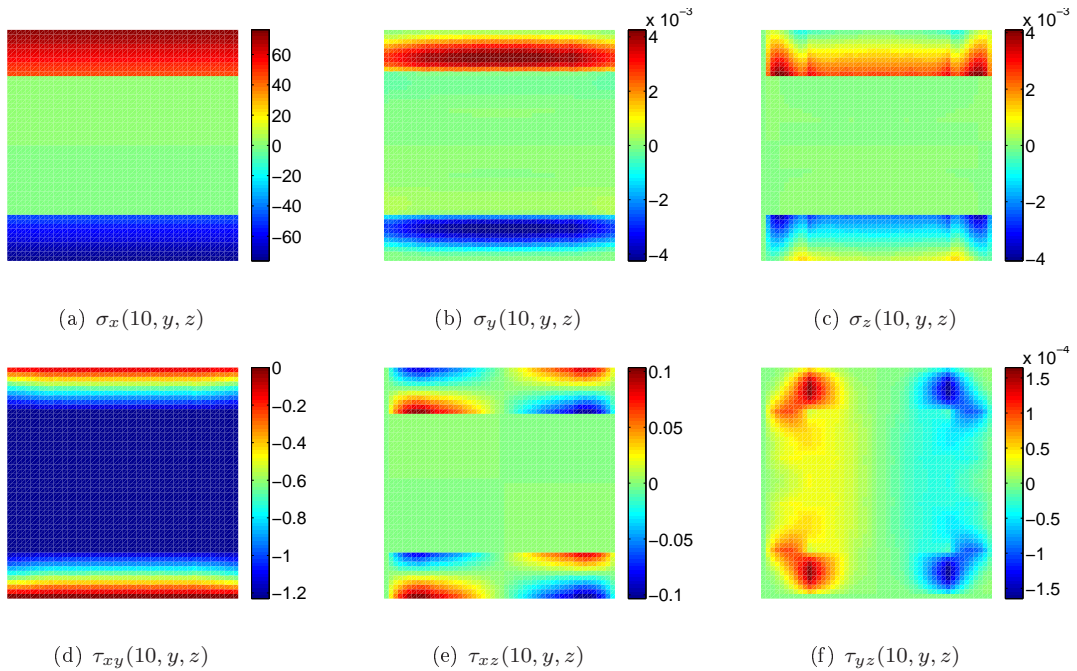


Figure 11: Stress distributions evaluated at  $x = 10\text{mm}$  for the non homogeneous case.

	MB FE		ABAQUS	
	min	max	min	max
$\sigma_x$	$-7.54 \cdot 10^1$	$7.54 \cdot 10^1$	$-7.55 \cdot 10^1$	$7.55 \cdot 10^1$
$\sigma_y$	$-5.73 \cdot 10^{-2}$	$5.73 \cdot 10^{-2}$	$-2.57 \cdot 10^{-1}$	$2.57 \cdot 10^{-1}$
$\sigma_z$	$-1.22 \cdot 10^{-1}$	$1.22 \cdot 10^{-1}$	$-3.36 \cdot 10^{-1}$	$3.39 \cdot 10^{-1}$
$\tau_{xy}$	$-1.23 \cdot 10^0$	$0.00 \cdot 10^0$	$-1.23 \cdot 10^0$	$-8.01 \cdot 10^{-2}$
$\tau_{xz}$	$-1.25 \cdot 10^{-1}$	$1.25 \cdot 10^{-1}$	$-9.62 \cdot 10^{-2}$	$9.62 \cdot 10^{-1}$
$\tau_{yz}$	$-7.27 \cdot 10^{-3}$	$7.27 \cdot 10^{-3}$	$-1.02 \cdot 10^{-1}$	$1.02 \cdot 10^{-1}$

Table 5: Minimum and maximum value of stress components distributions evaluated on the cross-section  $x = 10\text{mm}$  for the non-homogeneous case, evaluated with different methods.

### 5.3. L-shape cross-section beam

We consider the cross-section geometry and fiber distribution reported in Figure 5(c). We assume the beam length, the axial mesh, and the displacement constraint of the example in Section 5.2, while the material parameters are set as  $E = 10^5\text{MPa}$  and  $\nu = 0.25$ . We load the beam with a torsion moment equal to  $1\text{Nmm}$  in  $A_l$ , imposed through a couple of opposite unit forces  $[0, 0, 1]\text{N}$  and  $[0, 0, -1]\text{N}$  applied in vertices  $(20, -0.5; -0.5)$  and  $(20, 0; 0.5)$  respectively. The stress distributions at  $x = 10\text{mm}$  are reported in Figure 12.

It is interesting to observe that, as expected, the magnitude of  $\sigma_x$ ,  $\sigma_y$ ,  $\sigma_z$  and  $\tau_{yz}$  is negligible with respect to the magnitude of the shear components  $\tau_{xy}$  and  $\tau_{xz}$ . Moreover, considering the cross-section symmetry highlighted in Figure 5(c), the  $\tau_{xy}$  distribution is anti-symmetric respect to the  $\tau_{xz}$  distribution. Finally, a small stress concentration of  $\sigma_x$ ,  $\sigma_y$ ,  $\sigma_z$  and  $\tau_{yz}$  can be appreciated close to the section vertices where concentrated forces are applied. **In order to validate the results, we compute a 3D numerical solution using the ABAQUS software and a homogeneous mesh of 40 brick elements. In Table 6 we report the minimum and the maximum values of the cross-section stress distribution evaluated on the cross-section  $x = 10\text{mm}$ . From the comparison of the two method results it is possible to appreciate the substantial agreement of the results. We notice a small difference between the maximum values of  $\tau_{xy}$  and  $\tau_{xz}$  that occurs in the reflex**

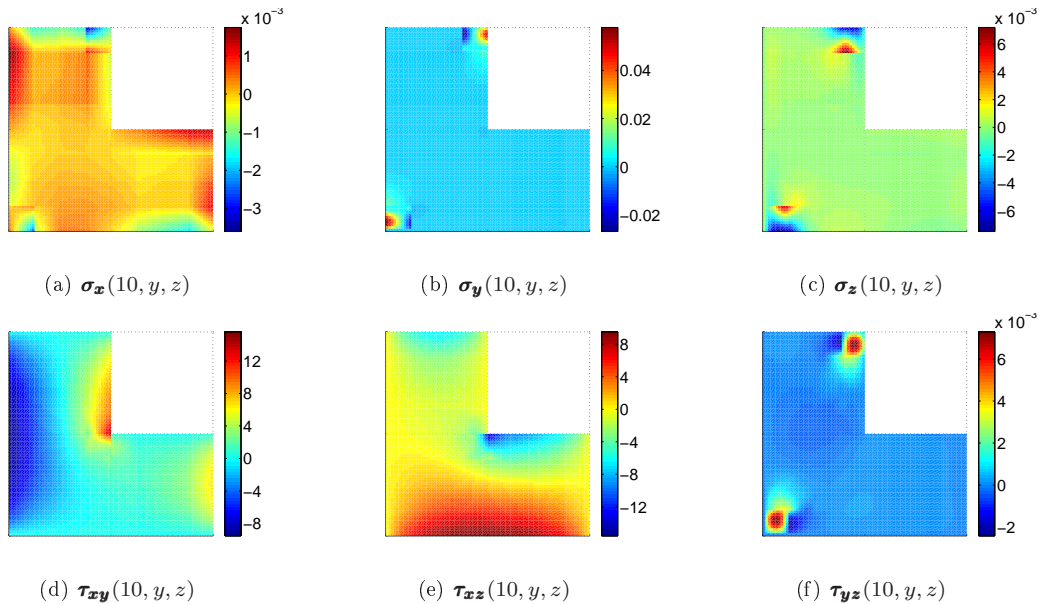


Figure 12: Stress distributions evaluated at  $x = 10\text{mm}$  for the L-shape cross section.

	MB FE		ABAQUS	
	min	max	min	max
$\sigma_x$	$-3.61 \cdot 10^{-3}$	$1.74 \cdot 10^{-3}$	$-1.20 \cdot 10^{-9}$	$1.65 \cdot 10^{-9}$
$\sigma_y$	$-2.68 \cdot 10^{-2}$	$5.78 \cdot 10^{-2}$	$-1.41 \cdot 10^{-11}$	$1.51 \cdot 10^{-11}$
$\sigma_z$	$-7.50 \cdot 10^{-3}$	$7.19 \cdot 10^{-3}$	$-1.49 \cdot 10^{-11}$	$2.12 \cdot 10^{-11}$
$\tau_{xy}$	$-9.54 \cdot 10^0$	$1.56 \cdot 10^1$	$-1.66 \cdot 10^1$	$9.55 \cdot 10^0$
$\tau_{xz}$	$-1.56 \cdot 10^1$	$9.54 \cdot 10^0$	$-9.55 \cdot 10^0$	$1.66 \cdot 10^1$
$\tau_{yz}$	$-2.47 \cdot 10^{-3}$	$7.29 \cdot 10^{-3}$	$-8.12 \cdot 10^{-12}$	$1.24 \cdot 10^{-11}$

Table 6: Minimum and maximum value of stress components distributions evaluated on the cross-section  $x = 10\text{mm}$  for the L-shape case, evaluated with different methods.

angle of the cross-section where stress concentration occurs.

## 6. Conclusions

In this paper we develop a 3D beam model methodology and possible corresponding FE schemes: starting from a suitable Hellinger-Reissner formulation of the elastic problem, we derive beam models by using a variational dimension reduction approach. When the profile functions are properly selected, the resulting models lead to ODEs systems that can capture the boundary effects, too. However, we do not discuss how to evaluate the warping functions and the generalized stress and displacements. Those aspects might be treated as illustrated in Dong et al. (2001).

Introducing a suitable FE discretization of the beam-model, we obtain a numerical scheme capable of accurately describing both displacement and stress fields, as the numerical results confirm.

Future developments of the present work could include: a rigorous mathematical study of the model; the development of more specific cross-section shape functions, with the aim to handle more general geometries; optimization issues, with the aim of reduce the number of involved DOFs; the consideration of more general constitutive laws.

## Acknowledgements

The authors were partially supported by the Italian MIUR through the PRIN Project n. 2010BFXRHS. This support is gratefully acknowledged.

## Bibliography

- Alessandrini, S. M., D. N. Arnold, R. S. Falk, and A. L. Madureira (1999). Derivation and justification of plate models by variational methods. *CRM Proceedings and Lecture Notes* 21, 1–20.
- Allix, O. and C. Dupleix-Couderc (2010). A plate theory as a mean to compute precise 3D solutions including edge effects and related issues. *New trends in thin structures: formulation, optimization and coupled problems*, 1–28.
- Auricchio, F., G. Balduzzi, and C. Lovadina (2010). A new modelling approach for planar beams: Finite-element solutions based on mixed variational derivations. *Journal of Mechanics of Materials and Structures* 5, 771–794.
- Batra, R., S. Vidoli, and F. Vestroni (2002). Plane wave solutions and modal analysis in higher order shear and normal deformable plate theories. *Journal of Sound and Vibration* 257, 63–88.
- Batra, R. C. and S. Vidoli (2002). Higher-order piezoelectric plate theory derived from a three-dimensional variational principle. *AIAA (American Institute of Aeronautics and Astronautics) journal* 40, 91–104.
- Brezzi, F. and M. Fortin (1991). *Mixed and hybrid finite element methods*. New York, NY, USA: Springer-Verlag New York, Inc.
- Ciarlet, P. (1997). *Theory of plates*, Volume 2. North Holland.
- Dong, S. B., J. B. Kosmatka, and H. C. Lin (2001). On Saint-Venant's problem for an inhomogeneous, anisotropic cylinder - part I: methodology for Saint-Venant solutions. *ASME, Journal of Applied Mechanics* 68, 376–381.
- Gruttmann, F., R. Sauer, and W. Wagner (1999). Shear stresses in prismatic beams with arbitrary cross-sections. *International journal for numerical methods in engineering* 45, 865–889.
- Hjelmstad, K. and E. Taciroglu (2002). Mixed methods and flexibility approaches for nonlinear frame analysis. *Journal of constructional steel research* 58, 967–993.
- Hjelmstad, K. and E. Taciroglu (2003). Mixed variational methods for finite element analysis of geometrically non-linear, inelastic Bernoulli-Euler beams. *Communications in numerical methods in engineering* 19, 809–832.
- Hjelmstad, K. D. (2005). *Fundamentals of structural mechanics*. Springer.
- Kantorovich, L. and V. Krylov (1958). *Approximate methods of higher analysis* (Third ed.). P. Noordhoff LTD.
- Kosmatka, J. B., H. C. Lin, and S. B. Dong (2001). On Saint-Venant's problem for an inhomogeneous, anisotropic cylinder - part II: cross-sectional properties. *ASME, Journal of Applied Mechanics* 68, 382–391.
- Lacarbonara, W. and A. Paolone (2007). On solution strategies to Saint-Venant problem. *Journal of Computational and Applied Mathematics* 206, 473–497.
- Ladeveze, P. and J. Simmonds (1998). New concepts for linear beam theory with arbitrary geometry and loading. *European Journal of Mechanics, A/solids* 17, 377–402.
- Lin, H. C., S. B. Dong, and J. B. Kosmatka (2001). On Saint-Venant's problem for an inhomogeneous, anisotropic cylinder - part III: end effects. *ASME, Journal of Applied Mechanics* 68, 392–398.
- Quarteroni, A., R. Sacco, and F. Saleri (2007). *Numerical Mathematics* Springer.
- Timoshenko, S. and J. N. Goodier (1951). *Theory of Elasticity* (Second ed.). McGraw-Hill.
- Vinayak, R., G. Prathap, and B. Naganarayana (1996). Beam elements based on a higher order theory – I formulation and analysis of performance. *Computers and Structures* 58, 775–789.
- Vogelius, M. and I. Babuska (1981a). On a dimensional reduction method I. The optimal selection of basis functions. *Mathematics of Computation* 37, 31–46.
- Vogelius, M. and I. Babuska (1981b). On a dimensional reduction method II. Some approximation-theoretic results. *Mathematics of Computation* 37, 47–68.